**Supplementary Information (SI) for ChemComm.**
**This journal is © The Royal Society of Chemistry 2025**

# Supplementary Information

## Co-MOFs incorporated $TiO_2$ nanorods for the photoelectrocatalytic decomposition of seawater aimed at hydrogen production and the concurrent synthesis of HClO

Chenhang Huangfu[a] ,Yuncai Song[a] ,Xiaohong Li[a], Wanggang Zhang[b], Jian Wang[b*], Yiming Liu[cde*]

*a College of Chemistry and Chemical Engineering, Taiyuan University of Technology, Taiyuan Shanxi, 030024, PR China.*

*b College of Materials Science and Engineering, Taiyuan University of Technology, Taiyuan Shanxi, 030024, PR China.*

*c School of Chemical Engineering and Technology, Taiyuan University of Science and Technology, Taiyuan, 030024, PR China.*

*d Shanxi Key Laboratory of Catalysis and Energy Coupling, Taiyuan University of Science and Technology, Taiyuan, 030024, PR China*

*e College of Environmental Science and Engineering, Taiyuan University of Technology, Taiyuan, 030024, PR China*

E-mail: JianWang: wangiian@tyut.edu.cn；Yiming Liu: liuym812@163.com

## 1. Materials and reagents

All chemicals utilized in the experiments were sourced from Sinopharm Chemical Reagent (Beijing Co., Ltd.) and were not subjected to any additional purification processes unless explicitly indicated. Deionized water was employed consistently throughout the experimental procedures. The reagents tetrabutyl titanate ($C_{16}H_{36}O_4Ti$), hydrochloric acid (HCl, 36.5-38 wt%), sodium chloride (NaCl), and cobalt nitrate hexahydrate ($Co(NO_3)_2 \cdot 6H_2O$) were procured from Sinopharm Chemical Reagent (Beijing Co., Ltd.). The fluorine-doped tin oxide (FTO) substrate utilized in the experiments exhibited a resistance of 7 Ω, a transmittance of 80%, and dimensions of 15 × 15 × 2.2 mm, and was supplied by Japan Plate Glass Co. Ltd.

### 2. Synthesis of $TiO_2$ nanorods

Titanium dioxide ($TiO_2$) nanorod arrays were synthesized utilizing a conventional hydrothermal technique. Initially, fluorine-doped tin oxide (FTO) substrates underwent ultrasonic cleaning in a solution comprising acetone, alcohol, and deionized water for a duration of 30 minutes, followed by drying in a vacuum oven. Subsequently, a solution was formulated by combining 7.5 mL of hydrochloric acid (38 wt%) with 7.5 mL of deionized water, which was stirred for 10 minutes before the gradual addition of 0.25 mL of tetrabutyl titanate. This mixture was then stirred for an additional 30 minutes. The dried FTO substrate, oriented with the conductive side facing upwards, was positioned at the bottom of a polytetrafluoroethylene (PTFE) lined autoclave. The prepared mixture was poured over the substrate, and the autoclave was assembled and sealed. The system was subsequently heated to 160°C for a period of 12 hours, after which it was allowed to cool naturally to room temperature. Following the cooling process, the FTO substrates, now coated with $TiO_2$ nanorods, were subjected to cleaning, drying, and final annealing in air at 450°C for 3 hours to produce $TiO_2$ photoanodes.

### 3. Synthesis of xCo-MOFs/$TiO_2$ nanorod composite photoanodes

A mixture consisting of 32 ml of DMF, 2 ml of ethanol, and 2 ml of water was prepared in a 100 ml beaker. Subsequently, 0.75 mmol of p-phthalic acid was dissolved in the mixed solution under sonication. Following this, cobalt nitrate hexahydrate ($Co(NO_3)_2 \cdot 6H_2O$) was introduced at varying concentrations of 0.01, 0.03, 0.05, 0.07, and 0.09 mol/L. The synthesized $TiO_2$ photoanode, oriented with the conductive side facing upwards, was positioned within a polytetrafluoroethylene (PTFE) liner, and the mixed solution was subsequently poured over it. The entire assembly was then sealed within an autoclave and subjected to hydrothermal treatment at a temperature of 140 °C for a duration of 48 hours. Finally, the resultant xCo-MOFs/$TiO_2$ composite was thoroughly washed with deionized water and ethanol.[1]

### 4. Characterization

The morphology of the samples was examined utilizing field emission scanning-electron microscopy (FE-SEM, TESCAN MIRA3 LMH) at an accelerating voltage of 10 kV. Characterization of the samples was conducted through high-resolution transmission electron microscopy (HRTEM) and selected area electron diffraction (SAED) measurements, in conjunction with energy dispersive X-ray spectroscopy (EDS), employing a field emission transmission electron microscope (TEM, JEOL2100F) at an accelerating voltage of 200 kV. X-ray diffraction (XRD, Rigaku Smartlab) was performed on the samples

using Cu Kα radiation within a 2θ range of 5 to 80 degrees. The valence states and elemental composition of the samples were analyzed viaX-ray photoelectron spectroscopy (XPS, ESCALAB 250Xi) utilizing Al Kα radiation.Additionally, UV-Vis diffuse reflectance spectra were assessed using a PerkinElmer Lambda 750 UV-Vis spectrometer.

**5. Photoelectrochemical measurements**

To assess the electrochemical performance, a three-electrode configuration was employed, interfaced with a Metrohm Autolab (PGSTAT302N) electrochemical workstation. A series of experiments were conducted, including transient photocurrent measurements (I-t) against photocurrent and a standard calomel electrode (SCE) at a potential of 0.5938 V, electrochemical impedance spectroscopy (EIS) at the same potential relative to the SCE, and linear sweep voltammetry (LSV) tests conducted within a potential range of -0.5 to 1.5 V with respect to the SCE. All experiments werecarried out in a simulated seawater electrolyte solution containing 3.5% NaCl. To replicate solar radiation conditions, a 300 W xenon lamp (Perfect Light) was utilized in conjunction with an AM 1.5G filter, providing an intensity of 100 mW $cm^{-2}$. It is important to note that all potentials referenced in this study were converted to values relative to the reversible hydrogen electrode (RHE), and these values were expressed in volts according to the specified equation[2]：

$$E_{RHE} = E_{calomel} + E^{0}{}_{calomel} + 0.059pH$$

The incident photon current conversion efficiency (IPCE) was measured using aPLS-MC300 monochromator (Perfect Light) in conjunction with a plx-ssx300 xenon lamp (Perfect Light). The calculation of IPCE was performed as follows[3]：

$$IPCE = \frac{1240}{\lambda} * (J_{dark} - J_{light}) * 100\%$$

The applied bias photocurrent efficiency (ABPE) is determined from the linear sweep voltammetry (LSV) curve utilizing the following formula：

$$ABPE = J \times (1.23 - V_{bias}) \; P \times 100\%$$

**6. Marine Hydrogen Evaluation**

Under typical reaction conditions, the photoanode was submerged in an H-type quartz electrolytic cell filled with a 3.5% aqueous sodium chloride solution. The hydrogen evolution process was conducted under AM 1.5 G illumination (100mW/$cm^2$)for a duration of 6 hours, during which a constant potential of 1.23 V versus the reversible hydrogen electrode (RHE) was maintained at ambient temperature (~298 K)

**7. Concentration of HClO by iodometric method**

Under typical reaction conditions, the photoanode was submerged in an H-type quartz electrolytic cell filled with a 3.5% NaCl aqueous solution. The hydrogen evolution process was conducted under AM 1.5 G illumination (100mW/$cm^2$) for a duration of 6 hours, during which a constant potential of 1.23 V versus the reversible hydrogen electrode (RHE) was maintained, alongside a controlled ambient temperature of approximately 298 K.

A volume of twenty milliliters of electrolyte solution obtained from the reacted anode was collected for analysis. Initially, an excess of potassium iodide (KI) solution was introduced to the sample. The addition of potassium iodide supplies iodide ions ($I^-$), resulting in the formation of iodine monomer ($I_2$) through a chemical reaction.

$$HClO + I^- \rightarrow I^2 + Cl^-$$

At this stage, iodine monomers are generated within the solution, exhibiting yellow or brown hues.

The iodine monomer ($I_2$) obtained is subsequently subjected to titration using a standardized sodium thiosulfate ($Na_2S_2O_3$) solution. Throughout the titration process, the iodine monomers undergo a reaction with sodium thiosulfate, resulting in the reduction of iodine monomers to iodide ions ($I^-$). This reaction is accompanied by a gradual lightening of the solution's color.

$$I^2 + 2Na_2S_2O_3 \rightarrow 2NaI + Na_2S_4O_6$$

The endpoint of the titration reaction is achieved when the iodine monomers present in the solution are entirely reduced. At this juncture, a noticeable color change occurs, transitioning the solution from brown to colorless. The determination of the titration endpoint can be facilitated by this color change, and the addition of a starch indicator is commonly employed to enhance visibility of the endpoint. The interaction between starch and iodine monomers results in the formation of a blue complex; as the iodine monomers undergo reduction, the blue hue of the solution progressively diminishes. The titration is considered complete when the blue color has completely vanished.

Determination of Concentration: The concentration of hypochlorite in a sample can be ascertained through stoichiometric calculations based on the volume of sodium thiosulfate solution utilized, which is of a known concentration.

$$[HClO] = C_{Na_2S_2O_3} * \frac{V_{Na_2S_2O_3}}{2} / V_{sample}$$

$C_{Na_2S_2O_3}$is the concentration of sodium thiosulfate.

$V_{Na_2S_2O_3}$is the volume of sodium thiosulfate consumed during the titration (L)

$V_{sample}$is the volume of solution sampled (L)

**8. Morphological and structural characterization of photoanodes**

The xCo-MOFs/$TiO_2$ composite photoanodewas synthesized utilizing a two-step hydrothermal approach, as illustrated in Fig.S1. Initially, $TiO_2$ nanorod arrays were fabricated on fluorine-doped tin oxide (FTO) substrates through a combination of hydrothermal treatment and subsequent annealing. Following this the FTO glass containing the $TiO_2$ nanorod arrays was immersed in a solution containing cobalt nitrate ($Co(NO_3)_2$, and the assembly was subjected to hydrothermal conditions at 140 °C for a duration of 48 hours within a high-pressure reactor. Subsequently, the FTO glass was thoroughly rinsed with deionized water and dried for six hours to yield various molar concentrations of x Co-MOFs/$TiO_2$. The process was repeated, wherein the FTO glass with $TiO_2$ nanorod arrays was again immersed in a cobalt nitrate solution and subjected to hydrothermal treatment at 140 °C for 48 hours. After removal from the autoclave, the glass was rinsed with deionized

water and dried for an additional six hours, resulting in the formation of xCo-MOFs/$TiO_2$ composites with differing molar concentrations.

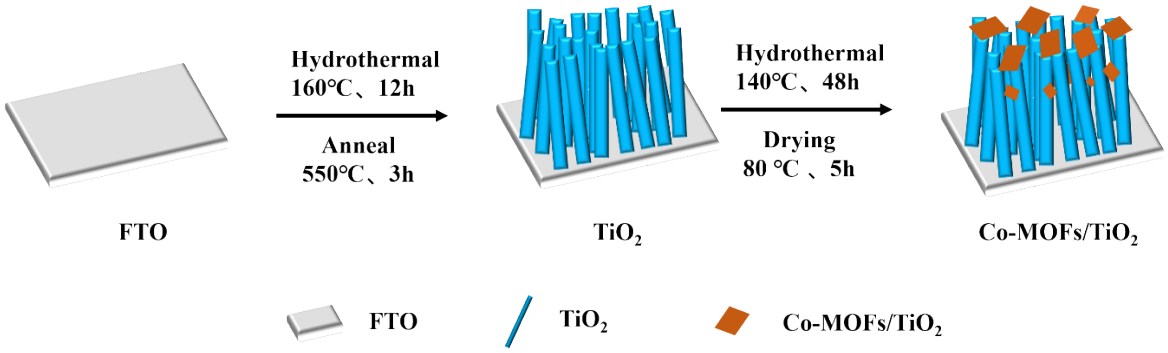


**Fig.S1**. The schematic synthetic route of the composite photoanode Co-MOFs/$TiO_2$

In Fig.S2(a), titanium dioxide ($TiO_2$) nanorods, approximately 400 nm in diameter, were uniformly deposited onto a fluorine-doped tin oxide (FTO) glass substrate. The hydrothermal method was utilized to incorporate cobalt metal-organic frameworks (Co-MOFs) onto the $TiO_2$ nanorods[4], as depicted in Fig.S2(b). The Co-MOFs, introduced at a concentration of 0.05 mol/L $Co(NO_3)_2$, exhibited a uniform tetragonal morphology on the $TiO_2$ nanorods. Transmission electron microscopy (TEM) images of the 0.05 Co-MOFs/$TiO_2$ composite photoanode, shown in Fig.S2(c), further confirm the successful deposition of Co-MOFs onto the $TiO_2$ nanorods. Additionally, the TEM energy-dispersive spectroscopy (EDS) images presented in Fig.S2(d) clearly indicate the presence of titanium (Ti), cobalt (Co), and oxygen (O) elements within the 0.05 Co-MOFs/$TiO_2$ composite, thereby providing further evidence of the successful and uniform incorporation of Co-MOFs onto the $TiO_2$ nanorods and the effective synthesis of the Co-MOFs/$TiO_2$ composite photoanodes.

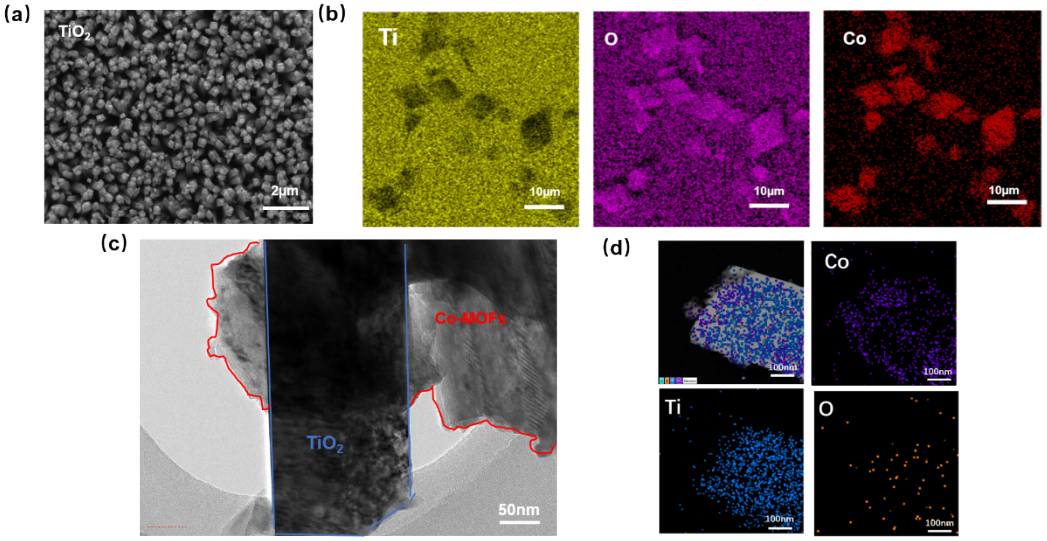


**Fig.S2** (a) SEM image of $TiO_2$ nanorods (b) EDS image of 0.05Co-MOFs/$TiO_2$ (c) TEM image of 0.05Co-MOFs/$TiO_2$ (d) STEM-EDS image

The chemical bonding states of Co-MOFs/$TiO_2$ were analyzed using XPS, with the findings presented in Fig.S3(a) to (d). The comprehensive spectrum validates the presence

of cobalt (Co), oxygen (O), and titanium (Ti) (Fig.S3a), which aligns well with the elemental mapping results obtained from energy-dispersive spectroscopy (EDS) (Fig.S2b, d). As illustrated in Fig. S3(b), the two prominent peaks observed at 780.7 eV and 796.9eV are indicative of the Co $2p_{3/2}$ and Co $2p_{1/2}$ orbitals, respectively. Additionally, the satellite peaks at 786.9 eV and 803.3 eV further substantiate the existence of the $Co^{2+}$ oxidation state within the material. XPS analysis of the O1s region (Fig. S3c) reveals that the primary peak at 529.78 eV is linked to M-O lattice oxygen, while the peak at 531.69 eV indicates a localized electronic state change due to an oxygen vacancy defect ($O_v$). The oxygen vacancy peak at 531.5 eV in the O 1s spectrum of pure $TiO_2$ is similar to the oxygen vacancy concentration found in the Co-MOFs/$TiO_2$ composites, suggesting that adding Co-MOFs does not significantly alter the oxygen vacancy concentration in the $TiO_2$ matrix. Additionally, a minor peak at 532.1 eV is associated with surface chemisorbed hydroxyl groups (-OH). It is important to note that oxygen vacancies can greatly influence the energy band structure of the material, improve the separation of photogenerated carriers, and create more active sites for catalytic reactions, thereby enhancing photoelectrocatalytic performance. The double peaks at 458.53 eV and 464.23 eV in the Ti 2p spectra (Fig. S3d) correspond to Ti $2p_{3/2}$ and Ti $2p_{1/2}$, respectively, with binding energies that align with the characteristics of the $TiO_2$ rutile phase. In summary, these results confirm the successful creation of Co-MOFs/$TiO_2$ composite photoanodes.[5-9]

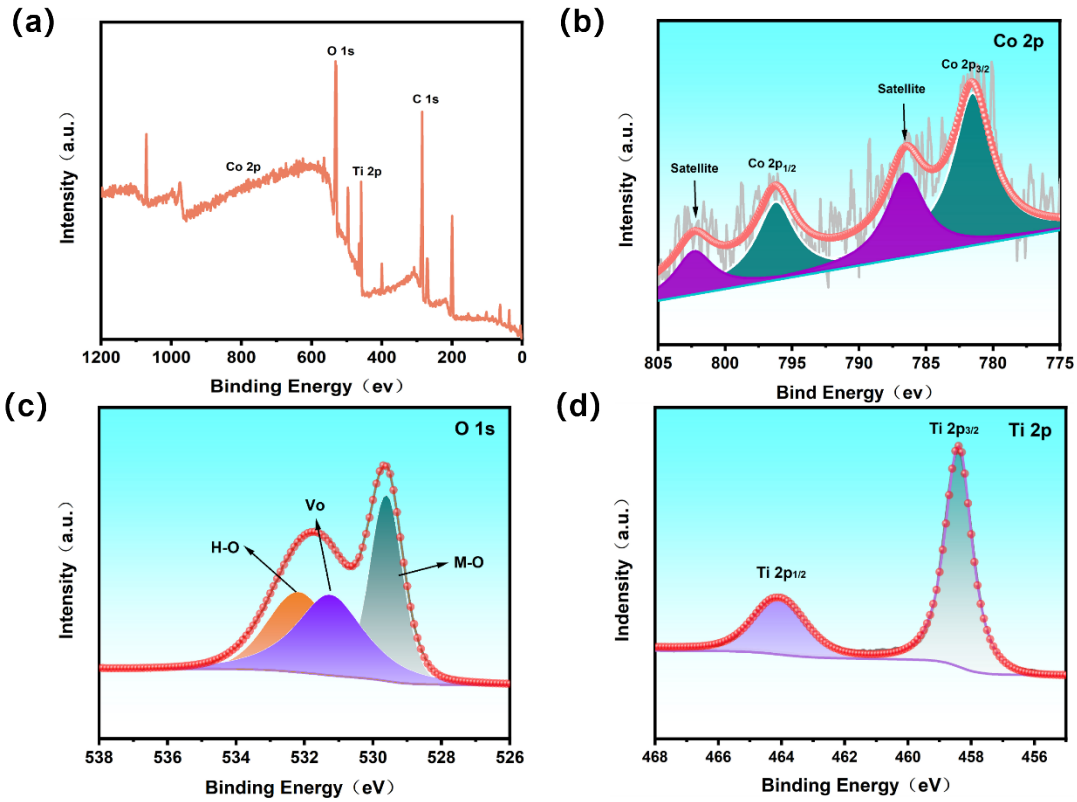


**Fig.S3** (a) xps full spectrum of 0.05Co-MOFs/$TiO_2$ (b)-(d) narrow spectra of Co2p, O1s and Ti2p

**9. Photoelectrochemical properties of photoanodes**

The photoelectrocatalytic performance of various photoanodes was evaluated in a simulated seawater electrolyte (3.5% NaCl) under conditions mimicking sunlight (AM 1.5G, 150mW/cm²). The photocurrent response curves (refer to Fig.S4a) were recorded at an applied potential of 1.23 V versus the reversible hydrogen electrode (RHE) for a duration of 300 seconds. The findings indicated that pure $TiO_2$ exhibited the lowest photocurrent density of 0.5 mA/cm². In contrast, the photocurrent densities of the xCo-MOFs/$TiO_2$ samples were markedly higher. Notably, the 0.05 Co-MOFs/$TiO_2$ sample achieved a photocurrent density of 1.5 mA/cm², which is threefold greater than that of the pure $TiO_2$ nanorod arrays. This enhancement may be attributed to the insufficient loading of Co-MOFs when the Co source is minimal, resulting in negligible modification of $TiO_2$, whereas excessive Co source leads to an overload of Co-MOFs, consequently diminishing the active surface sites of $TiO_2$[10]. Fig.S4(b) presents the transient photocurrent response, revealing that all photoanodes exhibit minimal photocurrent density in the absence of light, with significant fluctuations in photocurrent intensity corresponding to the photoperiod, suggesting a substantial generation of photogenerated electrons under illuminated conditions.

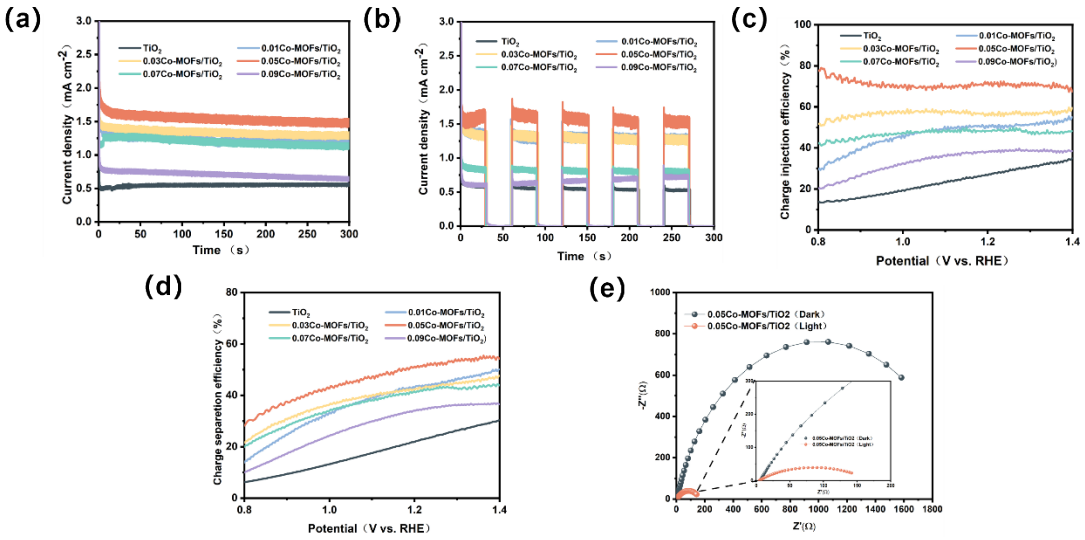


**Fig.S4** (a) Time-photocurrent curves of $TiO_2$, xCo-MOFs/$TiO_2$. (b) Transient photocurrent (i-t) curves (c) Surface charge injection efficiency of electrodes (d) Charge separation efficiency (e) Electrochemical impedance spectra (EIS) of 0.05Co-MOFs/$TiO_2$ under light and dark conditions

The efficiencies of charge injection and charge separation are influenced by the presence of the hole trapping agent, sodium sulfite ($Na_2SO_3$). As illustrated in Fig.S4(c), the charge injection efficiency of the 0.05 Co-MOFs/$TiO_2$ composite reaches 70% at a potential of 1.23 V versus the reversible hydrogen electrode (RHE), in contrast to the 25% efficiency observed for the pure $TiO_2$ photoanode under the same conditions. This suggests that the modified composite photoanode exhibits enhanced composite efficiency and accelerated charge transfer. Furthermore, as depicted in Fig.S4(d), the charge separation efficiency of the 0.05 Co-MOFs/$TiO_2$ photoanode at 1.23 V vs RHE is 58%, significantly higher than the 20% efficiency of the pure $TiO_2$ photoanode[11]. These findings indicate that the strong

interaction between $TiO_2$ nanorods and Co-MOFs promotes rapid charge transfer at the electrode/interface.

Moreover, the radius of the EIS curves for the 0.05 Co-MOFs/$TiO_2$ photoanode under illuminated conditions was markedly smaller than that observed under dark conditions[12]. This observation suggests that the illumination facilitates the release of electrons from the photoanode's surface, thereby enhancing the conductivity of the electrolyte solution and effectively diminishing the charge transfer resistance, as depicted in Fig.S4(e).

**10. Testing of natural seawater**

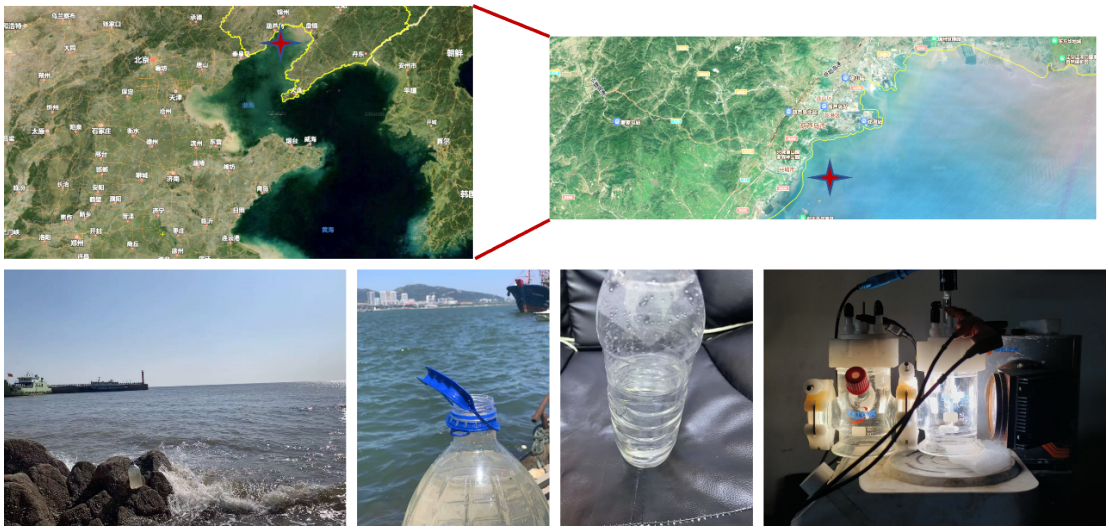

**Fig.S5** Genuine seawater source and trial images.

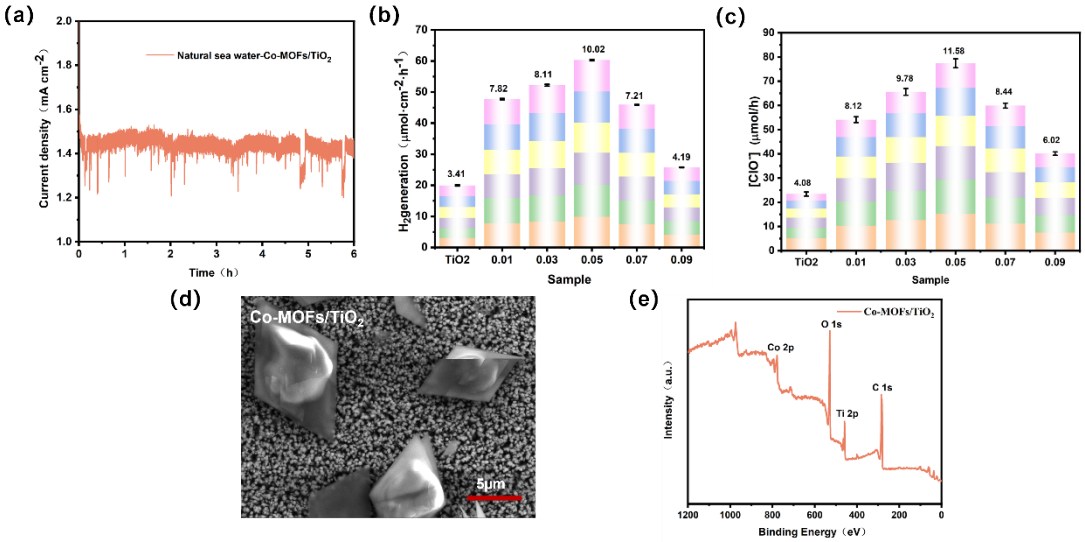


**Fig.S6** (a) Stability of photoelectric current in actual seawater for a duration of 6 hours (b) Along with the average hydrogen production rate (c) The rate of hypochlorous acid generation over the same period. (d) Scanning image of 0.05Co-MOFs/$TiO_2$ after real seawater reaction (e) Full spectrum of xps after real seawater reaction of 0.05Co-MOFs/$TiO_2$

Research on photocurrent and the production rates of hydrogen and hypochlorite in natural seawater showed that the photocurrent measured 1.4 mA/cm$^2$ over a duration of 6 hours, as illustrated in Fig. S6(a). The hydrogen production rate was 10.02 μmol/cm$^2$/h, while hypochlorite production reached 11.58 μmol/h during the same period, as depicted in Fig. S6(c). These figures indicate a decrease of approximately 7% compared to simulated seawater (3.5% NaCl), with a similar reduction in the average rates of photocurrent and hydrogen production observed in natural seawater sourced from the Bohai Sea, China. Additionally, hypochlorite production rates also experienced a decline of 6-7%. Despite this, the overall efficiency remained relatively high at around 93%. The post-reaction scanning image in Fig. S6（d）shows no visible fouling on the composite photoanode's surface, and the full spectrum analysis via post-reaction XPS in Fig. S6(e) did not reveal the presence of elements like Ca or Mg. Notably, the minimal efficiency loss (<10%) suggests that the 3.5% NaCl solution serves as an appropriate simplified model for the preliminary assessment of materials decomposed in seawater, especially for evaluating intrinsic activity trends related to short-term stability.

**11. Stability of catalysts**

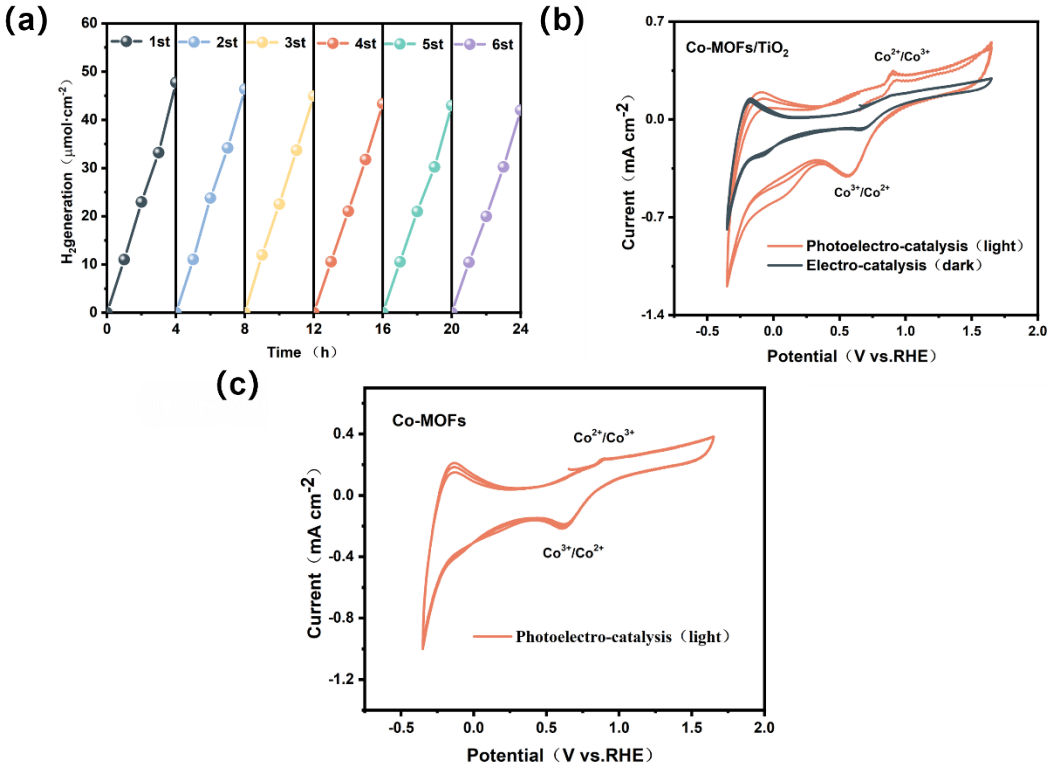


**Fig.S7** (a) Stability of hydrogen production of 0.05Co-MOFs/$TiO_2$ for 26 cycles (b) Cyclic voltammetry (CV) curves of 0.05Co-MOFs/$TiO_2$ under dark and light conditions (c) Cyclic voltammetry (CV) profiles of pure cobalt metal-organic frameworks (Co-MOFs)

Fig.S7(a) illustrates the stabilization performance of the 0.05 Co-MOFs/$TiO_2$ composite photoanodes across six consecutive four-hour cycles. As depicted in Fig.S7(b), distinct redox peaks associated with the $Co^{2+}/Co^{3+}$ transition are observable under dark conditions. In contrast, under illuminated conditions, these peaks demonstrate notable shifts in position

and an increase in intensity, indicating that photogenerated charge carriers play an active role in facilitating the redox process, a finding that aligns with prior studies [13]. Importantly, our comparative analysis with pure Co-MOFs (Fig.S7c) reveals that, while the cyclic voltammetry curves exhibit comparable redox characteristics, the peak shapes are considerably broadened and the intensity of the response is diminished relative to the composite system. This observation implies that the distinctive structure of the composites enhances the optimization of charge transport pathways. Furthermore, the redox-active $Co^{2+}/Co^{3+}$ species interact synergistically with other components within the composite system, significantly enhancing the anodic oxidation of $Cl^-$ ions, as evidenced by the increased oxidation currents and stable potential responses. The catalytic efficiency of the composite system surpasses that of the pure Co-MOFs, as confirmed by the observed enhancements in oxidation current and potential stability.

**12. Type II heterogeneous structure construction**

The light absorption characteristics of the composite photoanodes were assessed utilizing UV-visible diffuse reflectance spectroscopy (UV-visible), as illustrated in Figure S8(a). The findings indicate that the pure $TiO_2$ photoanodes, due to their substantial bandgap, are limited to absorbing ultraviolet light with wavelengths less than 424 nm, corroborating previous research. The incorporation of Co-MOFs into the composite enhanced the absorption intensity across various wavelengths. Employing the Kubelka-Munk function, we determined the bandgaps of $TiO_2$ and Co-MOFs to be 3.0 eV and 2.7 eV, respectively (refer to Fig.S8b). Additionally, ultraviolet photoelectron spectroscopy (UPS) was conducted to analyze the energy band structures of $TiO_2$ and Co-MOFs. The results revealed that the Fermi energy levels for $TiO_2$ and Co-MOFs were -4.57 eV and -4.81 eV, with corresponding valence band positions of 2.78 eV and 2.38 eV, respectively (see Figures S8c and S8d). Consequently, we identified the cascade effect of Co-MOFs/$TiO_2$ heterostructures when exposed to sunlight. The energy band positions of the Co-MOFs/$TiO_2$ system are characteristic of type II heterojunctions. Under dark conditions, an interfacial electric field is established between the Co-MOFs and $TiO_2$, resulting in energy band bending. Subsequently, upon light excitation, the applied electric field and the band bending facilitate the transfer of photogenerated electrons from the conduction band of Co-MOFs to the conduction band of $TiO_2$, while the photogenerated holes in the valence band of $TiO_2$ migrate to the valence band of Co-MOFs. Thus, the formation of a type II heterojunction between Co-MOFs and $TiO_2$ significantly mitigates electron-hole recombination and enhances carrier separation efficiency[14-15].

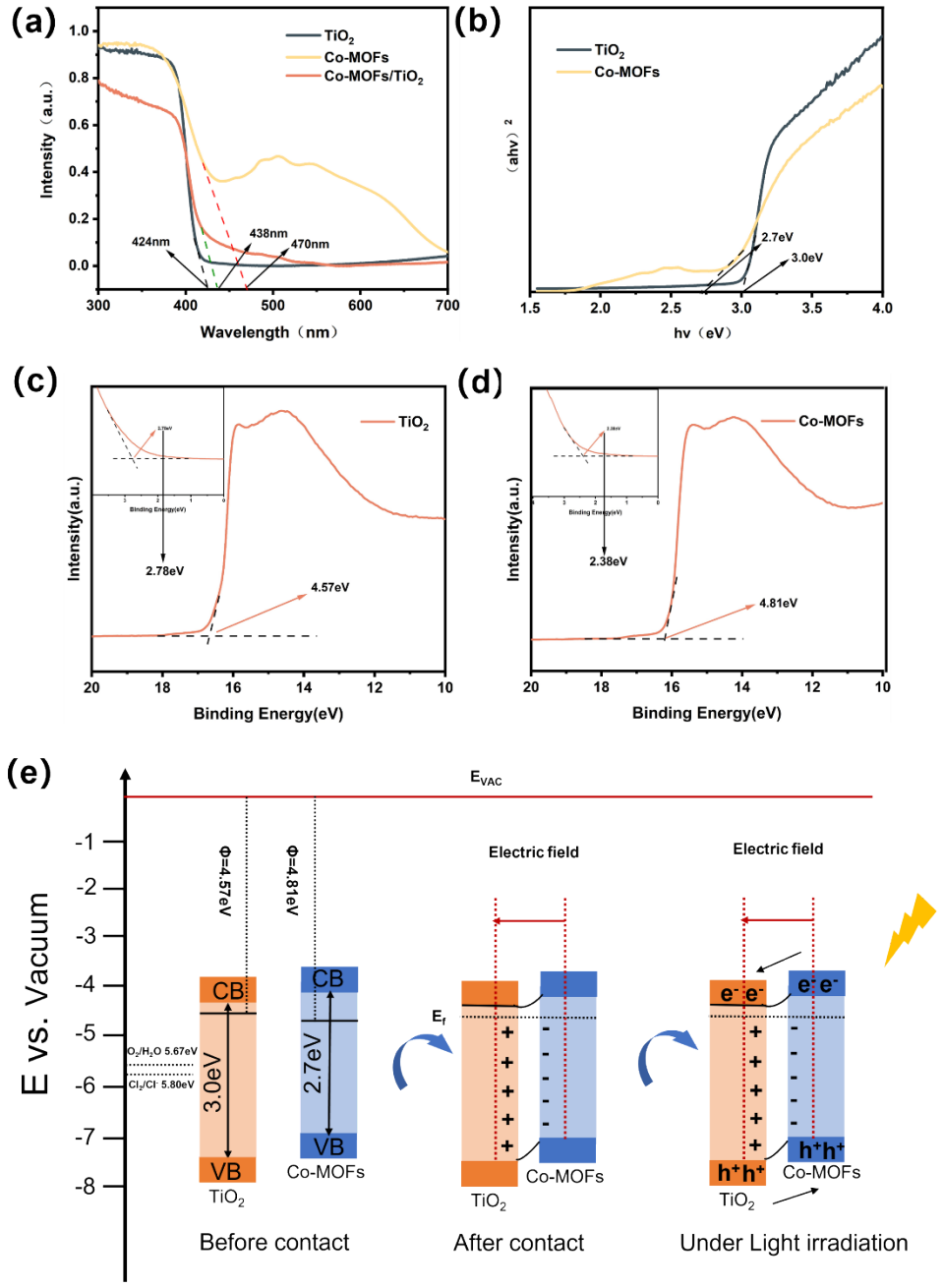


**Fig.S8** (a)UV-diffuse reflectance spectra of $TiO_2$, 0.05Co-MOFs/$TiO_2$, and Co-MOFs (b) forbidden bandwidth plots of $TiO_2$, Co-MOFs (c)-(d) figure of the figure of merit function and valence band spectra of $TiO_2$ and Co-MOFs (e) schematic diagram of the energy band structures of Co-MOFs/$TiO_2$

**13. Hydrogen and hypochlorite mechanisms in marine waters**

In this research, we effectively developed a photoelectrocatalytic anode material utilizing a Co-MOFs/$TiO_2$ heterojunction and investigated its catalytic mechanism in the decomposition of seawater. The heterostructure formed between Co-MOFs and $TiO_2$ markedly improves the separation efficiency of photogenerated charge carriers and enhances

photoelectrocatalytic a ctivity, leading to the efficient production of hypochlorous acid alongside significant hydrogen generation.

Hydrogen production from seawater transpires at the cathode, while the Co-MOFs/$TiO_2$ composite photoanode facilitates the absorption of photon energy. This process results in the excitation of electrons from the valence band to the conduction band. Subsequently, the electrons accumulate at the conduction band of $TiO_2$ and are transferred to the anode, where they participate in the hydrogen evolution reaction, driven by the application of a bias voltage.

$$2H^+ + 2e^- = H_2$$

At the anode, chloride ions ($Cl^-$) represent the most prevalent and easily oxidized anions found in seawater. Although the thermodynamic oxidation of water ($O_2/H_2O$, 1.23 V vs SHE at pH = 0) is more favorable than the oxidation of chloride ions ($Cl_2/Cl^-$, 1.36 V vs SHE at pH = 0), the kinetics of the reactions suggest otherwise. The oxidation of $Cl^-$ is a two-electron process, which occurs more efficiently compared to the four-electron process involved in the oxidation of water to oxygen. Following the photoexcitation of electrons, a significant number of holes are generated in the valence band of the cobalt metal-organic frameworks Co-MOFs/$TiO_2$ composite photoanode. Consequently, chlorine precipitation is expected at the anode, as the oxidation potential of the valence band of Co-MOFs (2.18 V vs SHE) is substantially higher than the oxidation potential of chloride ions (1.36 V vs SHE).

$$2Cl^- + 2h^+ \rightarrow Cl_2$$

$$Cl_2 + H_2O \rightarrow H^+ + Cl^- + HClO$$

$$Cl^- + 2OH^- \rightarrow ClO^- + H_2O$$

In the anode region, water molecules participate in a four-electron transfer process facilitated by the catalytic properties of Co-MOFs/$TiO_2$：

$$4OH^- \rightarrow O_2 + 2H_2O + 4e^-$$

## 14. References


1. W. Han, X. Huang, G. Lu and Z. Tang, Catal Surv Asia, 2018, 23；64-89.

2. D. Chen, Z. Liu, Z. Guo, W. Yan and Y. Xin, J. Mater. Chem. A, 2018, 6;20393–20401.

3. D. Chen, Z. Liu, Z. Guo, W. Yan and M. Ruan, Chem Eng J, 2020,381,122655.

4. S. Shen, J. Chen, M. Wang, X. Sheng, X. Chen, X. Feng and S. S. Mao, Prog Mater Sci, 2018, 98, 299-385.

5.Y. Wang, M. Kong, Z. Liu, C. Lin and Y. Zeng, J. Mater. Chem. A,2017,46,24269–24274;

6.Q. Wang, J. He, Y. Shi, S. Zhang, T. Niu, H. She, Y. Bi and Z. Lei, Appl Catal B-Environ, 2017, 214, 158-167;

7.Y. Feng, L. Ling, Y. Wang, Z. Xu, F. Cao, H. Li and Z. Bian, Nano Energy, 2017,40,481-486;

8. X. Huang, X. Gao, Q. Xue, C. Wang, R. Zhang, Y. Gao and Z. Han, Dalton Trans, 2020, 49, 2184-2189.

9. D. Pal, D. Maity, A. Sarkar, D. Sarkar and G. G. Khan, J. Colloid Interface Sci, 2022, 620, 209-220.

10. J. Yu, J. Gonzalez-Cobos, F. Dappozze, F. J. Lopez-Tenllado, J. Hidalgo-Carrillo, A. Marinas, P. Vernoux, A. Caravaca and C. Guillard, Appl Catal B-Environ, 2022, 318, 121843.

12. J. Sun, H. Wu, C. Fu, C. Zhang, Z. Hu and M. Zhou, Appl Catal B-Environ, 2024, 351, 123976.

13. T.-J. Wang, X. Liu, Y. Li, F. Li, Z. Deng and Y. Chen, Nano Res, 2020, 13, 79-85.

14. M. A. U. Olea, J. d. J. P. Bueno and A. X. M. Perez, JECE, 2021, 9, 106480;

15. Li, J. Yao, Q. Yu, X. Zhang, S. A. Carabineiro,X. Xiong, C. Wu and K. Lv, Appl Catal B-Environ, 2024, 351, 123950.

16.W. Luo, Z. Yang, Z. Li, J. Zhang, J. Liu, Z. Zhao, Z. Wang, S. Yan, T. Yu and Z. Zou, Energy Environ. Sci, 2011, 4, 4046-4051.

17.Y. Li, J. Feng, H. Li, X. Wei, R. Wang and A. Zhou, Int J Hydrogen Energy, 2016, 41, 4096-4105.

18.R.-T. Gao, X. Guo, S. Liu, X. Zhang, X. Liu, Y. Su and L. Wang, Appl Catal B-Environ 2022, 304, 120883.

19.X. Guo, X. Liu and L. Wang, J. Mater. Chem. A, 2022, 10, 1270-1277.

20.J. Liu, S.-M. Xu, Y. Li, R. Zhang and M. Shao, Appl Catal B-Environ, 2020, 264, 118540.